Lithuanian Journal of Physics, Vol. **60**, No. 3, pp. 172–184 (2020)

PHOTOLUMINESCENCE PROPERTIES OF HYBRID PEROVSKITES IN SOLAR CELLS WITH TiO_2 AND $Mg_{0.2}Zn_{0.8}O$ ELECTRON TRANSPORT LAYERS

A. Čerškus [a, b], **S. Ašmontas** [a], **K. Petrauskas** [a], **A. Sužiedėlis** [a], **J. Gradauskas** [a, b],

A.S. Opanasyuk [c], **and B. Vengalis** [a]

[a] *State Research Institute Center for Physical Sciences and Technology, Savanorių 231, 02300 Vilnius, Lithuania*
[b] *Vilnius Gediminas Technical University, Saulėtekio 11, 10223 Vilnius, Lithuania*
[c] *Sumy State University, 2 Rymskogo-Korsakova St., 40007 Sumy, Ukraine*
Email: aurimas.cerskus@ftmc.lt

Received 28 November 2019; revised 3 February 2020; accepted 17 March 2020

This paper presents a study of the photoluminescence properties of hybrid perovskite films deposited on titanium and magnesium zinc oxide films, as electron transport layers, using the spin-coating technique. The subject of the investigation was continuous wave photoluminescence versus temperature, excitation power and transient photoluminescence. Moreover, the paper discusses possible carrier recombination mechanisms. Complex temporal decay was approximated through the use of several models, but only the four-exponent model and the model using the sum of two hyperbolic functions provided a good agreement with the experimental data. The first attempt to replace titanium dioxide with magnesium zinc oxide in conjunction with the perovskite layer showed improved optical properties such as a weaker non-radiative recombination process and a longer decay time constant.

PACS: 81.10.Dn, 84.60.Jt, 78.55.-m, 78.47.D-

Keywords: perovskite, solar cell, photoluminescence, time resolved spectroscopy

1. Introduction

In recent years, hybrid organic–inorganic metal halide perovskite OMX_3 (O = organic cation, M = metal cation, X = halide anion) materials have gained popularity as promising candidate materials for efficient light-energy conversion devices [1]. Also, they have been reported to be potential materials for light-emitting devices [2, 3], lasers [4, 5] and field effect transistors [6]. Perovskites have attracted a significant attention due to their remarkable characteristics, such as excellent properties for transporting both electrons and holes [7, 8], their high efficiency for photoelectric conversion and high luminescence efficiency [9]. Another attractive feature of hybrid perovskites as photovoltaic absorbers is the continuous tunability of their bandgap energy, obtained by substituting the central organic molecule or metal and alloying different halides into the structure. An easy and relatively inexpensive method for the deposition of perovskites offers the possibility of large-scale solar cell production. During six years of research, the efficiency of perovskite solar cells to convert power has increased from less than 5% to more than 22% [1, 10]. Despite this impressive performance, perovskites have not as yet revealed their full potential. For instance, the photoluminescence (PL) quantum efficiency of thin films, used in highly efficient devices, is still far from unity [11]. Some issues such as moisture resistance and thermal stability [12, 13], light degradation [14–16], current-voltage (*J*-*V*) hysteresis [17, 18] and bandgap blue shifts with an increase of temperature [11, 19, 20] have not yet been fully resolved for these materials. Therefore, there still exists a great interest in deepening the study and the development of more stable perovskites films, more effective solar cells and other devices based on them.

Perovskite solar cells of a typical *n-i-p* architecture demonstrate the inherent hysteresis of *J-V* characteristics due to parasitic accumulation effects [21]. Meanwhile, the use of an inverse *p-i-n* structure significantly reduces the hysteresis effect [22]. Also, the change of charge transport layer material [23–27], as well as additives in the perovskite [18], can reduce the *J-V* hysteresis. Titanium dioxide (TiO_2) and zinc oxide (ZnO) are the inorganic electron transport materials (ETMs) most often used in the preparation of organic–inorganic hybrid perovskite solar cells [1]. Zhuang et al. used ZnO nanorods as ETM [20].

In this paper, we report the results of a study of photoluminescence on hybrid organic–inorganic metal halide perovskite films deposited by the spin-coating technique both on TiO_2 and magnesium zinc oxide ($Mg_{0.2}Zn_{0.8}O$) as electron transport layers (ETL). This work focuses on the investigation of continuous wave photoluminescence and on the time-resolved intrinsic photoluminescence properties of such perovskite films over a wide range of temperatures (from liquid helium to room temperature) as well as under various values of excitation power.

2. Sample fabrication and experimental details

Both types of samples were fabricated on fluorine-doped transparent conducting tin dioxide (FTO) coated glass substrates, sized 25 by 25 mm^2. Before deposition, the FTO surfaces were washed with ethanol and purified in an ultrasonic bath. The TiO_2 layers were comprised of two layers, compact and porous ones. The compact TiO_2 layers were deposited using the pyrolysis method. A titanium diisopropoxide bis(acetylacetonate) solution (75% in 2-propanol) diluted in ethanol in a 1:9 volume ratio was then sprayed on the 723 K temperature substrates and subsequently annealed in air for 15 min. Having cooled to room temperature, the porous TiO_2 layers were then deposited by the spin-coating method at 4000 rpm for 20 s using a TiO_2 paste diluted in ethanol (1:6, weight ratio). The layers were then sintered at 723 K in air for 15 min. The $Mg_{0.2}Zn_{0.8}O$ thin layers were deposited on FTO using the pulsed spray-pyrolysis method. A water solution of magnesium chloride ($MgCl_2{\cdot}6H_2O$) and zinc acetate ($Zn(CH_2CO_2)_2{\cdot}2H_2O$) in a concentration of 0.10 M was used as the precursor. The bulk content of initial components of the solution during the application of films was $x = 0.2$. The distance between the nozzle and glass substrates was 20 cm. The dispersed precursor particles were blown off with a 0.25 MPa air flow. Synthesis of the thin layers was carried out at 673 K substrate temperature.

Perovskite films were deposited on all the samples by the one-step spin-coating method from one solution in nitrogen atmosphere (<0.5 ppm O_2, <0.5 ppm H_2O). The solution was produced by dissolving formamidinium iodide (FAI) (1 M), lead iodide (PbI_2) (1.1 M), methylammonium bromide (MABr) (0.2 M) and lead bromide ($PbBr_2$) (0.2 M) in a 1:4 solution of dimethyl sulfoxide (DMSO) and N,N-dimethylformamide (DMF). 5% of the cesium iodide (CsI) solution (predissolved as a 1.5 M stock solution in DMSO) was then added to the prepared solution. The coating process involved a two-step procedure: 1000 rpm for 10 s and 6000 rpm for 30 s. Before the end of the spin-coating procedure, 150 μl of chlorobenzene was poured on the perovskites for 10 s. Then the layers were annealed at 383 K for 1 h. Having cooled down to room temperature, the 2,2′,7,7′-Tetrakis[N,N-di(4-methoxyphenyl)amino]-9,9′-spiro-bifluorene (Spiro-OMeTAD) layers were spin-coated at 4000 rpm for 20 s, during that time the Spiro-OMeTAD (60 mM) in a 1 ml chlorobenzene solution was applied with the addition of 28.8 μl 4-tert-butylpyridine (TBP) and 17.5 μl lithium bis(trifluoromethanesulfonyl)imide (Li-TFSI), predissolved as a 1.8 M stock solution in acetonitrile. Lastly, 80-nm-thick gold electrodes, used for the electrical measurements, were deposited onto the devices through a shadow mask by thermal evaporation. In this way, two types of mesoscopic heterojunction perovskite solar cells, having typical *n-i-p* structures, further referred to as samples S1, with the TiO_2 layers, and S2, containing $Mg_{0.2}Zn_{0.8}O$ layers, were prepared. The detailed structure of these solar cells is shown in Fig. 1.

The continuous wave (CW) PL spectra were measured using a standard photoluminescence setup with a fully automated 1-m focal length monochromator (FHR-1000), thus achieving a spectral dispersion of 0.8 nm/mm. The PL system resolution was 0.3 meV

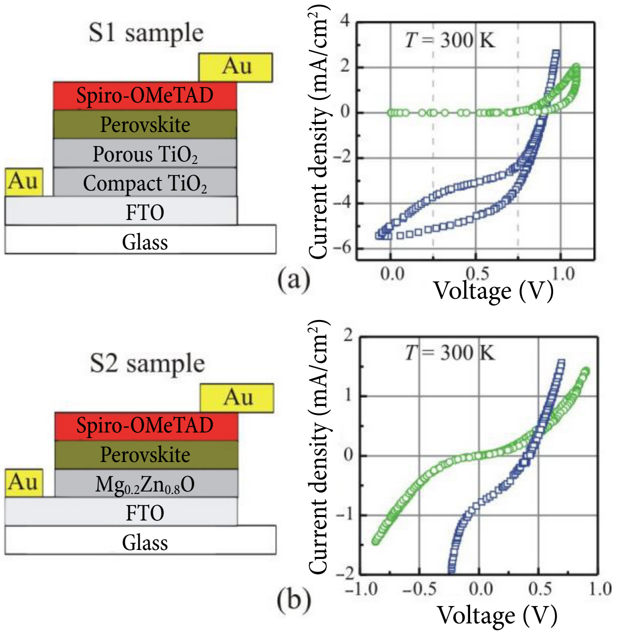

Fig. 1. The structure of the solar cells and their *J-V* characteristics in the dark (green circles online) and under 1 sun illumination (blue squares online) of (a) sample S1 with the TiO_2 layer and (b) sample S2 with the $Mg_{0.2}Zn_{0.8}O$ layer.

at the spectrum maximum for most measurements and did not exceed 0.8 meV at the lowest laser power. An Ar-ion laser was used as an excitation source. The excitation energy was in a region of 2.2–2.7 eV and its power was changed either with the help of power supply or by using neutral glass filters. The size of the laser spot on the surfaces of samples was 2.5 mm. Photoluminescence was detected with a thermoelectrically cooled gallium arsenide (GaAs) photomultiplier (H7421-50) operating in the photon counting regime. The temperature of the samples was changed from room temperature to 3.6 K by means of a closed-cycle helium optical cryostat.

The time-resolved (TR) PL measurements were performed using a pulsed 532 nm (photon energy 2.3 eV, repetition rate 10 kHz) diode pumped solid state (DPSS) microchip laser with a full width at a half maximum (FWHM) pulse of 400 ps. The PL was detected with a thermoelectrically cooled high-efficiency extended-red multi-alkali cathode photomultiplier (PMC-100-20) with an internal GHz preamplifier. The transient PL was measured using a time correlated single photon counting (TCSPC) system. The current–voltage characteristics of solar cells were measured using a standard measurement equipment (*Keithley* 2602A), and 100 mW/cm^2 irradiance was achieved by means of a AM1.5 spectral lamp (*Newport* model 67005), placed at an appropriate distance. The *J-V* characteristics are also presented in Fig. 1. It should be noted that samples S2 showed smaller *J-V* hysteresis, but lower values of short-circuit current and open-circuit voltage.

3. Experimental results and discussion

The CW PL spectra of the S1 and S2 samples, measured within a temperature range from 4 up to 300 K and at the Ar-ion laser excitation power density $I = 28$ mW/cm^2, are shown in Figs. 2 and 3, respectively. The PL integrated intensity, as a function of the reciprocal temperature, is depicted in the insets of these figures. The PL intensity of the S1 sample

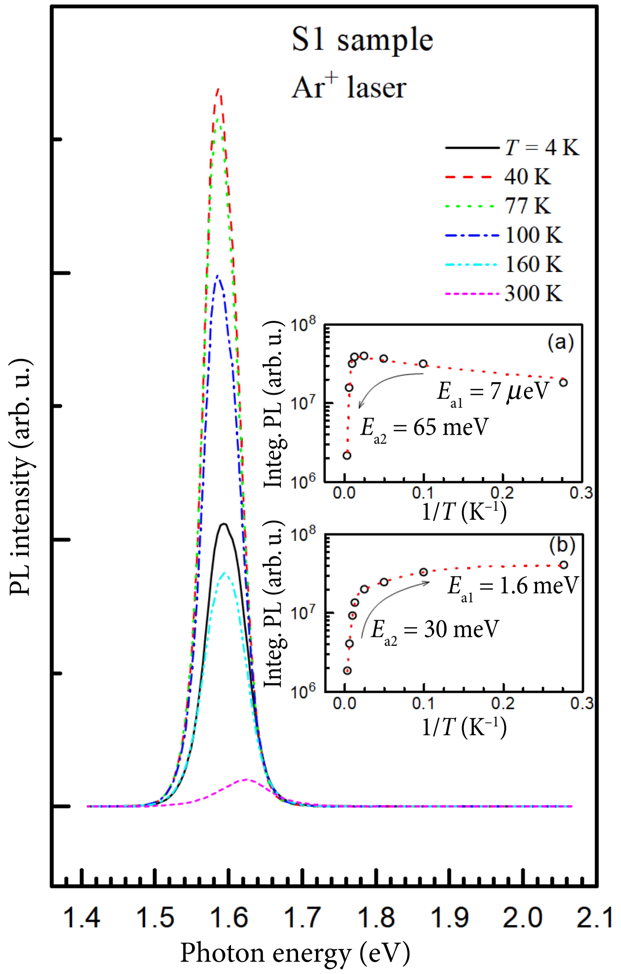

Fig. 2. The PL spectra of sample S1 with a TiO_2 layer recorded at different temperatures ranging from 4 to 300 K and at laser excitation power density $I = 28$ mW/cm^2. The insets show the Arrhenius plots of the integrated luminescence under conditions of (a) increasing and (b) decreasing temperature. The arrows indicate the direction of temperature change.

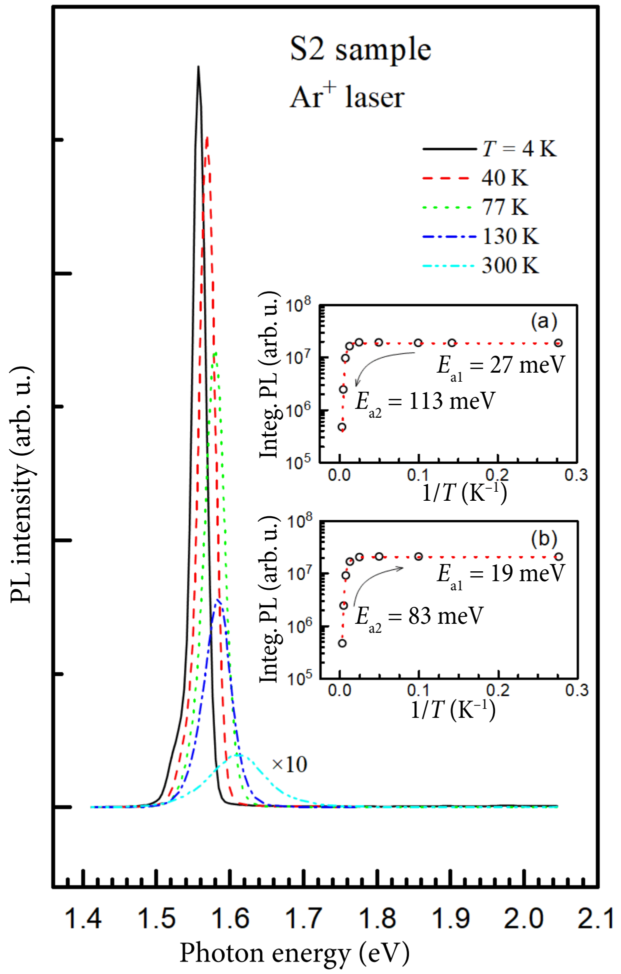

Fig. 3. The PL spectra of sample S2 with a $Mg_{0.2}Zn_{0.8}O$ layer recorded at different temperatures ranging from 4 to 300 K and at laser excitation power density $I = 28$ mW/cm². The insets show the Arrhenius plots of integrated luminescence under conditions of (a) increasing and (b) decreasing temperatures. The arrows indicate the direction of temperature change.

increased in temperatures up to 40 K (Fig. 2, inset (a)). A more detailed analysis showed that such an increase in intensity was accompanied by a shift of the peak maximum to the lower energy side (red shift) by about 10 meV. A further temperature rise up to 300 K caused a PL intensity decrease with a blue shift of the peak maximum decreasing by about 40 meV. Meanwhile, for sample S2, it continued to decrease with the rise of temperature, demonstrating about a 50 meV maximum blue shift. As the temperature dropped from 300 to 4 K, only an increase of the PL intensity (see insets (b) in Figs. 2 and 3) and a shift of the peak maximum to the lower energy side by about 27 and 50 meV were observed for samples S1 and S2, respectively. The inclusion of a different crystal phase, an atmosphere effect and a degradation of the sample, reabsorption effects, radiative recombination involving shallow trapping levels and luminescence from the crystal edges [28] could all be possible reasons for the red shift. We attributed this red shift to the relative change between the intensities of the two lowest energy peaks. If a recombination via a dominant non-radiative defect was quenched due to the thermal emission, we would see a simultaneous rise of PL intensity of another line [29]. This would explain the unusual tendency of the Arrhenius plot (inset (a) in Fig. 2). To fit the temperature-dependent PL intensities well, the Arrhenius plot of the PL integrated intensity was taken into consideration for two non-radiative recombination channels shown as in [30, 31]

$$I_{\mathrm{PL}}(T)=\frac{I_{\mathrm{PL}}(0)}{1+C_1\exp(-E_{\mathrm{a}1}/k_{\mathrm{B}}T)+C_2\exp(-E_{\mathrm{a}2}/k_{\mathrm{B}}T)}, \quad (1)$$

where C_1 and C_2 measured the strength of both quenching mechanisms, and E_{a1} and E_{a2} were the thermal activation energies in the low and high temperature regions, respectively. The fitting curves, based on Eq. (1), are displayed as red dashed lines in the insets of both measurement cases of increasing and decreasing temperatures (Figs. 2 and 3). The deduced thermal activation energies for both samples are summarised in Table 1. It can be seen that these values are mainly lower when the samples were cooled. Thus, we concluded that when the samples are heated or cooled, recombination takes place through different recombination paths. The energy values between 19 and 30 meV can be related to the thermal annihilation of an exciton. This is close to 20–24 meV exciton binding energy, determined from the absorption spectra [32]. A small difference (which is much higher than our system resolution) can appear, for example, due to strains [33]. Meanwhile, the higher energy values can be attributed to defects or

Table 1. The thermal activation energies evaluated using Eq. (1).

	S1 sample		S2 sample	
	E_{a1}, meV	E_{a2}, meV	E_{a1}, meV	E_{a2}, meV
T increase	0.007	65	27	113
T decrease	1.6	30	19	83

other changes in the crystalline structure [34]. The energy value 1.6 meV can be related to the localized states and the lowest value 0.007 meV is most likely due to the abovementioned two-line intensity change.

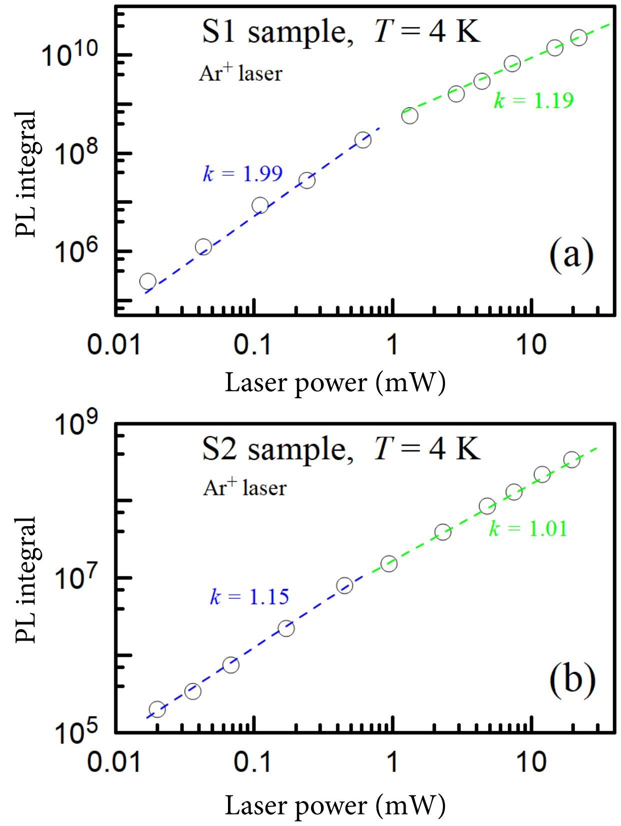

Fig. 4. Integrated PL intensity vs laser power (a) of sample S1 (with the TiO_2 layer) and (b) of sample S2 (with the $Mg_{0.2}Zn_{0.8}O$ layer), recorded at 4 K temperature. The dashed lines are the fitting results.

Figures 4 and 5 present the power-dependent PL results at 4 K temperature for samples S1 and S2, respectively. The laser power was varied by more than three orders of magnitude from a low to a medium excitation level. Log–log plots of the integral intensity of the PL spectra I_{PL} versus the exciting laser power P_{laser} help to identify the emission mechanisms. The dashed lines in Fig. 4 illustrate the power dependence of luminescence lines as $I_{PL} \sim P^k_{laser}$, which is correct when the P_{laser} value varies no more than by two orders of magnitude [35]. Accordingly, when the excitation light photon energy exceeds the forbidden energy gap E_g, then the coefficient $k = 2$ corresponds to the recombination of free carriers. $1 < k < 2$ signifies the exciton recombination (including free and localized excitons). The power index $k < 1$ indicates the cases of free-to-bound and donor–acceptor pair recombination processes. The change of k values proves that the excitonic emission is the dominating mechanism in both samples. The insignificant change of k from 1.15 to 1.01 (sample S2) is related to the increase of laser power. The power values averaged on a logarithmic scale are $P_{1laser} = 0.1$ mW for the range $P_{laser} = 0.02 - 0.8$ mW, and $P_{2laser} = 4.5$ mW for the range $P_{laser} = 0.8 - 25$ mW. The ratio P_{2laser}/P_{1laser} is equal to 45. Meanwhile, the $k = 1.19$ value of sample S1 corresponds to $x \approx 27$ (see Eq. (16) $k = \frac{2r}{2\sqrt{1+x}(-1+\sqrt{1+x})}$ or Fig. 1 in Ref. [36]). In that case, the value of x corresponding to $P_{1laser} = 0.1$ mW is given by $x \approx 27 \times P_{1laser}/P_{2laser} = 27/45 = 0.6$. The value of k at $x = 0.6$ is estimated to be about 1.8. The higher $k = 1.99$ value indicates that there also dominates a mechanism of free carrier recombination in sample S1 at a lower excitation level. Based on different changes in the k values, we concluded that the perovskite layers have different properties, such as radiative and competitive non-radiative recombination probabilities [36]. The laser excitation power and PL intensity are related to the recombination rates and the electron–hole concentration n as $P_{laser} \sim An + Bn^2 + Cn^3$ and $I_{PL} \sim Bn^2$. The power of laser excitation can be expressed as the power of PL intensity using the fitting parameters for each of the recombination processes (Shockley–Read–Hall, radiative and Auger) denoted as A_{PL}, B_{PL} and C_{PL} as follows [37–39]:

$$P_{laser} = A_{PL}(I_{PL})^{1/2} + B_{PL}I_{PL} + C_{PL}(I_{PL})^{3/2}. \quad (2)$$

The internal quantum efficiency can be directly determined experimentally [38]:

$$\eta_{int} = \left[1 + \frac{A_{PL}}{B_{PL}}(I_{PL})^{-1/2} + \frac{C_{PL}}{B_{PL}}(I_{PL})^{-1/2}\right]^{-1}. \quad (3)$$

Based on Eq. (2), the fitting results (dashed lines) and extracted fitting parameters A_{PL}, B_{PL} and C_{PL} are presented in Fig. 5. Although radiative recombination is obviously dominant in both samples, the non-radiative one, however, remains intense in sample S1. The maximum internal quantum efficiency values that were ascertained using Eq. (3) were 0.56 for sample S1 and 0.82 for sample S2. Consequently, we can draw the conclusion

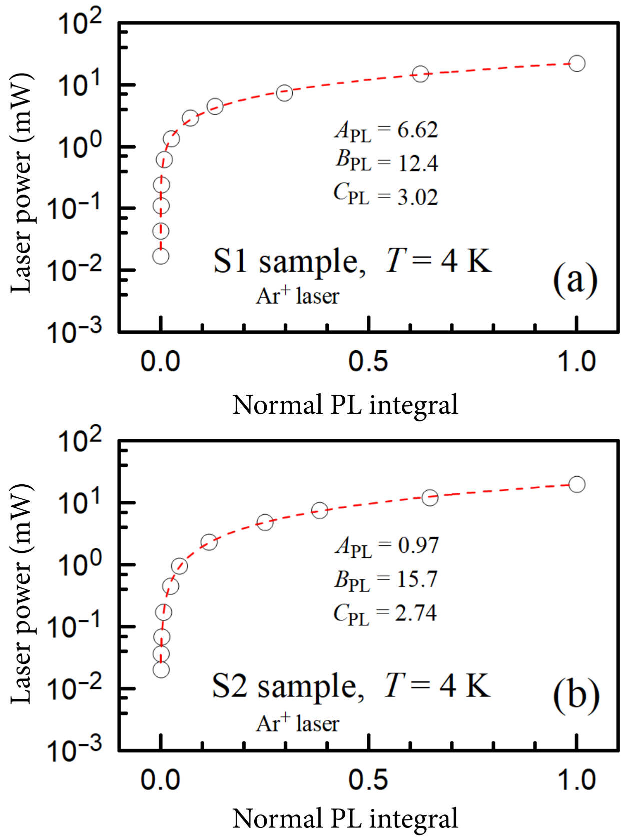

Fig. 5. Laser power vs normalized integrated PL intensity (a) of sample S1 (with the TiO_2 layer) and (b) of sample S2 (with the $Mg_{0.2}Zn_{0.8}O$ layer), recorded at 4 K temperature. The dashed lines are the fitting results according to Eq. (2).

that an optically better, i.e. demonstrating a weaker non-radiative recombination, perovskite layer has grown up on the ZnMgO layer.

The normalized PL spectra of both samples recorded at 300 K temperature using an Ar-ion CW laser (I = 100 mW/cm^2) or a pulsed DPSS microchip laser (I_{av} = 40 mW/cm^2) are shown in Fig. 6. These experimental results were fitted by three Gaussian functions (dotted lines). A clear structure of the spectra was observed when the samples were excited with the pulsed laser with an average excitation power density close to a half of one sun. In this case, much greater shifts to the low and high energy sides were observed as compared to those of the CW excitation case (see Fig. 6 and Table 2). This increase could be related to light induced modification [40] and efficient photon recycling [41].

After excitation with the CW laser, the difference between the first and second Gaussian peaks was 29 and 19 meV for samples S1 and S2, respectively. These peaks possibly correspond to the free exciton and band-to-band transitions. Also, the stronger contribution of the second Gaussian peak in sample S1 confirms the presence of free carrier recombination, thereby producing the biggest value of k and close to two. The distance between the second and third peaks is 62 and 7 meV for samples S1 and S2, respectively. A possible reason of this separation can be attributed to the presence of another phase of perovskite [42–44], different grain sizes [45] and emissions from the interior or boundaries of the grains [28, 45, 46]. However, the addition of small amounts of cesium (Cs) in a triple cation (Cs/MA/FA) configuration resulted in the formation of monolithic grains of a purer perovskite [47] and in the suppression of possible phase transitions [32]. Meanwhile, emissions from the interior and boundaries of the grains should show a different tendency of PL decay [28, 46]. An-

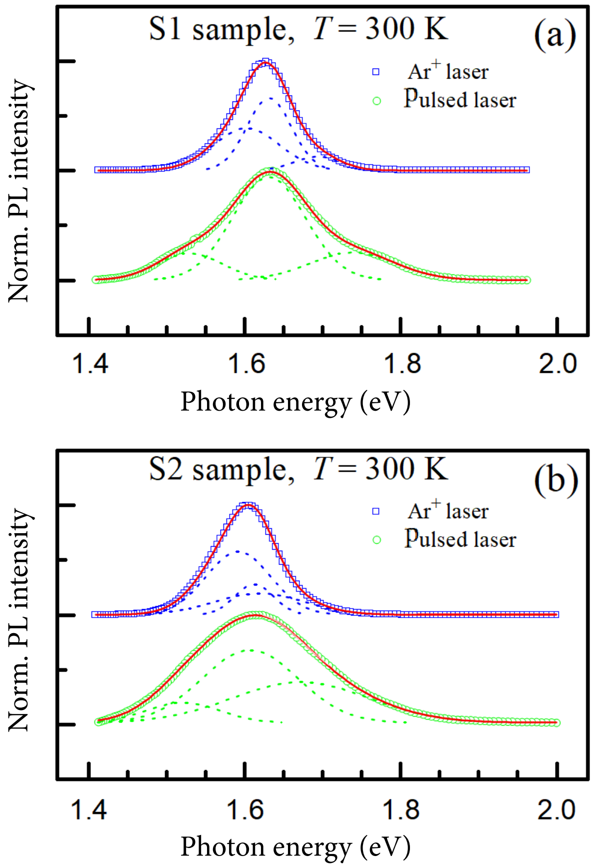

Fig. 6. The normalized PL spectra (a) of sample S1 (with the TiO_2 layer) and (b) of sample S2 (with the $Mg_{0.2}Zn_{0.8}O$ layer) recorded at 300 K temperature using a CW (I = 100 mW/cm^2) or a pulsed (I_{av} = 40 mW/cm^2) laser. The curves are offset vertically for clarity. The red (online) lines are the fitting results.

Table 2. The distances between the centres of Gaussian peaks.

	S1 sample			S2 sample		
	ΔE_{1-2}, meV	ΔE_{2-3}, meV	ΔE_{1-3}, meV	ΔE_{1-2}, meV	ΔE_{2-3}, meV	ΔE_{1-3}, meV
CW laser	29	62	91	19	7	27
Pulsed laser	99	108	207	86	65	151

other possible explanation for the presence of these three peaks could be the band edge and two kinds of local phases, distinguished as ordered and disordered crystallites [48]. However, this model cannot explain such different energies between the second and third Gaussian peaks. We thus assumed that the highest energy peak could be related to smaller-sized crystallites or to the residue of other phases. Some particular distances between the Gaussian peaks correlated well with thermal activation energy values derived earlier, e.g. 62 and 29 meV for sample S1 (see 65 and 30 meV in Table 1), and 19 and 27 meV for sample S2 (the same numerical values 19 and 27 meV in Table 1). This fact supported our conclusion that as the sample temperature increases and decreases, optical recombination occurs through two different paths. The other thermal activation energy values are related to the non-radiative recombination mechanism.

We measured the time-resolved PL decay curves in the centre and on both sides of the PL peak. The results were fitted by the multi-exponential function $I_{\mathrm{PL}}(t) = \Sigma A_i \mathrm{e}^{-t/\tau_i}$ and the amplitude weighted mean decay times were calculated as $\tau_{\mathrm{av}} = \frac{\Sigma A_i \tau_i}{\Sigma A_i}$. The transients appeared to be very complex, and only the 4-exponential model provided a good fit (the adjusted R-squared was 0.998 or higher, see the red fitting lines in Fig. 7). The extrapolated decay times ranged from 1 up to 108 ns with 3 to 5 time increments of magnitude. The average decay times at different spectral points were τ_{av} = 6.0, 9.6 and 10.6 ns for sample S1 (with TiO_2 layer) and τ_{av} = 7.8, 14.8 and 13.3 ns for sample S2 (with $Mg_{0.2}Zn_{0.8}O$ layer). Longer decay times also confirmed that the use of the MgZnO layer not only minimized the J-V hysteresis but also increased the optical quality of the perovskite in sample S2. Four decay times could be assigned to different recombination mechanisms [49] or interpreted with other models such as continuous Lorentzian lifetime distribution [50, 51], thermalized stretching of the exponential line shape [52], the stretched exponential (or Kohlrausch decay function), its modified versions according to Eq. (25) in Ref. [53] and Eq. (4) in Ref. [54], the stretched or compressed hyperbola (first described by E. Becquerel in the 1860s and known as the bimolecular decay model) [55–57] and as an alternative model [57]. However, neither of these models provided as good fitting results as the four-exponential approximation did.

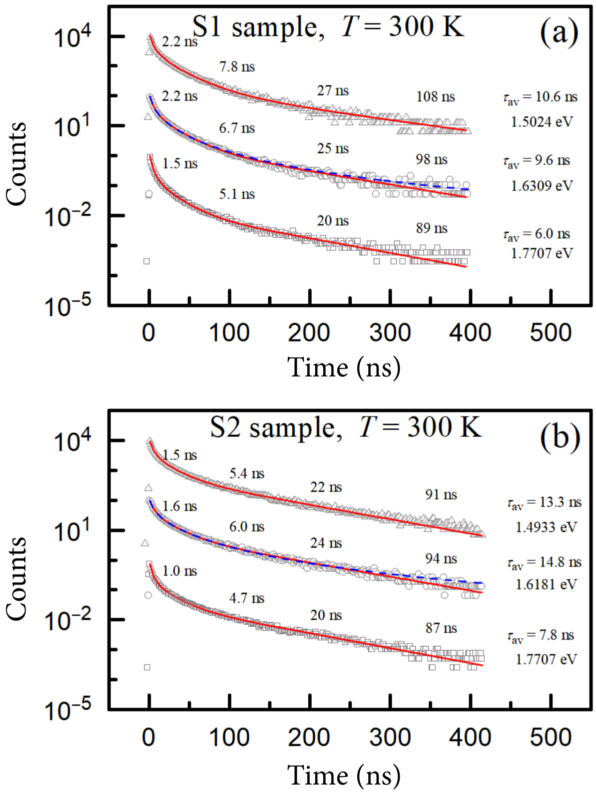

Fig. 7. PL decay transients at different spectral points (a) of sample S1 (with the TiO_2 layer) and (b) of sample S2 (with the $Mg_{0.2}Zn_{0.8}O$ layer). The curves are offset vertically for clarity. The solid red and blue (online) dashed lines are the fitting curves obtained using 4-exponential and double bi-molecular models, respectively.

The representation of experimental data in a negative time derivative of the PL intensity logarithm $-\frac{\mathrm{d}\ln I_{\mathrm{PL}}(t)}{\mathrm{d}t}$ as a function of the normalized PL intensity $\frac{I_{\mathrm{PL}}(t)}{I_{\mathrm{PL}}(t_0)}$ or of its square root $\frac{\sqrt{I_{\mathrm{PL}}(t)}}{\sqrt{I_{\mathrm{PL}}(t_0)}}$ can reveal some additional information about the recombination mode [58]. The results of $-\frac{\mathrm{d}\ln I_{\mathrm{PL}}(t)}{\mathrm{d}t}=f\left(\frac{I_{\mathrm{PL}}(t)}{I_{\mathrm{PL}}(t_0)}\right)$ revealed nearly linear dependence, while the $-\frac{\mathrm{d}\ln I_{\mathrm{PL}}(t)}{\mathrm{d}t}=f\left(\frac{\sqrt{I_{\mathrm{PL}}(t)}}{\sqrt{I_{\mathrm{PL}}(t_0)}}\right)$ function showed a clearly nonlinear dependence with two inclinations (we should note that the linear one related to the bi-molecular process). Finally, we approximated the PL decays as a double bi-molecular recombination process using the equation [56]

$$I_{\mathrm{PL}}(t)=\sum_i \alpha_i \frac{I_{\mathrm{PL}}(t_0)}{\left(1+\frac{c_i}{\tau_i}t\right)^{1/c_i}} \tag{4}$$

with two dimensionless parameters α_i and c_i, where $\Sigma\alpha_i = 1$. The average decay constant for the trace fitted by Eq. (4) was calculated accordingly [56]:

$$\tau_{\mathrm{av}}=\sum_i \frac{\alpha_i \tau_i}{1-c_i}. \tag{5}$$

An analysis of the complex decay with a sum of Becquerel functions produced good fitting results (adj. *R*-squared ⩾0.998, see blue dashed lines in Fig. 7). The average decay constant values calculated using Eq. (5) at the maximum of the PL peak were 11.4 and 17.6 ns for samples S1 and S2, respectively, and were a little higher than the ones ascertained by the multi-exponential model. The results of both fitting models are summarised in Table 3. The bi-molecular recombination could be a non-radiative recombination via a trap site, which accepts both electrons and holes, or a direct radiative recombination between an electron and a hole. Thus, this double bi-molecular recombination allows one to assume the presence of such type traps, other direct band-to-band recombinations or two different emissions from the interior and interfaces of such layer. However, this double bi-molecular recombination mechanism cannot explain the presence of three peaks, especially at the peak centre of sample S2.

4. Conclusions

We concluded that the perovskite layer, deposited on a MgZnO layer using spin-coating, demonstrates better optical properties, such as like non-radiative recombinations and longer decay times compared to the one grown on a TiO_2 layer. The temperature and laser power dependent perovskite PL measurements, as well as the PL decay analysis, prove the existence of two independent radiative recombination channels of an excitonic and bi-molecular character. Our estimations reveal that a complex analysis of the PL decay, assuming a 4-exponential model, can be replaced by the sum of two Becquerel functions. The first findings prove that MgZnO layers provide certain optical advantages and smaller *J*-*V* hysteresis. This also serves as motivation for further, more detailed studies of the magnesium zinc oxide layer as electron transport material for hybrid perovskite solar cells.

Acknowledgements

This work was supported in part by Research Council of Lithuania, Grants No. 01.2.2-LMT-K-718-01-0050 and No. S-LU-18-1. The authors are grateful to dr. Romanas Sedlickas for proofreading of the manuscript text and giving valuable comments and suggestions.

References

[1] P. Tonui, S.O. Oseni, G. Sharma, Q. Yan, and G.T. Mola, Perovskites photovoltaic solar cells: An overview of current status, Renew. Sustain.

Table 3. Fitting results of PL transients and χ^2 values.

Sample; position	4-exponential			Double bi-molecular		
	τ_{1-4}, ns	τ_{av}, ns	χ^2	$\tau_{1,2}$, ns	τ_{av}, ns	χ^2
S1; I	2.2, 7.8, 27, 108	10.6	0.210	2.8, 18	13.0	0.211
S2; I	1.5, 5.4, 22, 91	13.3	0.118	3.1, 18	15.2	0.137
S1; II	2.2, 6.7, 25, 98	9.6	0.146	3.0, 13	11.4	0.164
S2; II	1.6, 6.0, 24, 94	14.8	0.232	3.6, 21	17.6	0.237
S1; III	1.5, 5.1, 20, 89	6.0	0.045	2.0, 9.6	7.7	0.051
S2; III	1.0, 4.7, 20, 87	7.8	0.048	1.7, 13	10.3	0.062

Energy Rev. **91**, 1025–1044 (2018), https://doi.org/10.1016/j.rser.2018.04.069

[2] Q. Van Le, H.W. Jang, and S.Y. Kim, Recent advances toward high-efficiency halide perovskite light-emitting diodes: Review and perspective, Small Methods **2**(10), 1700419 (2018), https://doi.org/10.1002/smtd.201700419

[3] Y. Shang, Y. Liao, Q. Wei, Z. Wang, B. Xiang, Y. Ke, W. Liu, and Z. Ning, Highly stable hybrid perovskite light-emitting diodes based on Dion-Jacobson structure, Sci. Adv. **5**(8), eaaw8072 (2019), https://doi.org/10.1126/sciadv.aaw8072

[4] K. Wang, S. Wang, S. Xiao, and Q. Song, Recent advances in perovskite micro- and nano-lasers, Adv. Opt. Mater. **6**(18), 1800278 (2018), https://doi.org/10.1002/adom.201800278

[5] M. Stylianakis, T. Maksudov, A. Panagiotopoulos, G. Kakavelakis, and K. Petridis, Inorganic and hybrid perovskite based laser devices: a review, Materials **12**(6), 859 (2019), https://doi.org/10.3390/ma12060859

[6] X. Liu, D. Yu, X. Song, and H. Zeng, Metal halide perovskites: synthesis, ion migration, and application in field-effect transistors, Small **14**(36), 1801460 (2018), https://doi.org/10.1002/smll.201801460

[7] H. Oga, A. Saeki, Y. Ogomi, S. Hayase, and S. Seki, Improved understanding of the electronic and energetic landscapes of perovskite solar cells: high local charge carrier mobility, reduced recombination, and extremely shallow traps, J. Am. Chem. Soc. **136**(39), 13818–13825 (2014), pMID: 25188538, https://doi.org/10.1021/ja506936f

[8] T.M. Brenner, D.A. Egger, L. Kronik, G. Hodes, and D. Cahen, Hybrid organic–inorganic perovskites: low-cost semiconductors with intriguing charge-transport properties, Nat. Rev. Mater. **1**(1), 15007 (2016), https://doi.org/10.1038/natrevmats.2015.7

[9] I.L. Braly, D.W. deQuilettes, L.M. Pazos-Outón, S. Burke, M.E. Ziffer, D.S. Ginger, and H.W. Hillhouse, Hybrid perovskite films approaching the radiative limit with over 90% photoluminescence quantum efficiency, Nat. Photonics **12**(6), 355–361 (2018), https://doi.org/10.1038/s41566-018-0154-z

[10] M.A. Green, A. Ho-Baillie, and H.J. Snaith, The emergence of perovskite solar cells, Nat. Photonics **8**, 506–514 (2014), https://doi.org/10.1038/nphoton.2014.134

[11] S.D. Stranks, Nonradiative losses in metal halide perovskites, ACS Energy Lett. **2**(7), 1515–1525 (2017), https://doi.org/10.1021/acsenergylett.7b00239

[12] T.A. Berhe, W.-N. Su, C.-H. Chen, C.-J. Pan, J.-H. Cheng, H.-M. Chen, M.-C. Tsai, L.-Y. Chen, A.A. Dubale, and B.-J. Hwang, Organometal halide perovskite solar cells: degradation and stability, Energy Environ. Sci. **9**, 323–356 (2016), https://doi.org/10.1039/C5EE02733K

[13] K.K. Bass, R.E. McAnally, S. Zhou, P.I. Djurovich, M.E. Thompson, and B.C. Melot, Influence of moisture on the preparation, crystal structure, and photophysical properties of organohalide perovskites, Chem. Commun. **50**, 15819–15822 (2014), https://doi.org/10.1039/C4CC05231E

[14] P. Pistor, A. Ruiz, A. Cabot, and V. Izquierdo-Roca, Advanced Raman spectroscopy of methylammonium lead iodide: development of a non-destructive characterisation methodology, Sci. Rep. **6**, 35973 (2016), https://doi.org/10.1038/srep35973

[15] S. Ruan, M.-A. Surmiak, Y. Ruan, D.P. McMeekin, H. Ebendorff-Heidepriem, Y.-B. Cheng, J. Lu, and C.R. McNeill, Light induced degradation in mixed-halide perovskites, J. Mater. Chem. C **7**, 9326–9334 (2019), https://doi.org/10.1039/C9TC02635E

[16] G. Abdelmageed, L. Jewell, K. Hellier, L. Seymour, B. Luo, F. Bridges, J.Z. Zhang, and S. Carter, Mechanisms for light induced degradation in $MAPbI_3$ perovskite thin films and solar cells, Appl. Phys. Lett. **109**(23), 233905 (2016), https://doi.org/10.1063/1.4967840

[17] D.L. Jacobs, M.A. Scarpulla, C. Wang, B.R. Bunes, and L. Zang, Voltage-induced transients in methylammonium lead triiodide probed by dynamic photoluminescence spectroscopy, J. Phys. Chem. C **120**(15), 7893–7902 (2016), https://doi.org/10.1021/acs.jpcc.5b11973

[18] W. Ke, C. Xiao, C. Wang, B. Saparov, H.-S. Duan, D. Zhao, Z. Xiao, P. Schulz, S.P. Harvey, W. Liao,

W. Meng, Y. Yu, A.J. Cimaroli, C.-S. Jiang, K. Zhu, M. Al-Jassim, G. Fang, D.B. Mitzi, and Y. Yan, Employing lead thiocyanate additive to reduce the hysteresis and boost the fill factor of planar perovskite solar cells, Adv. Mater. **28**(26), 5214–5221 (2016), https://doi.org/10.1002/adma.201600594

[19] K. Wu, A. Bera, C. Ma, Y. Du, Y. Yang, L. Li, and T. Wu, Temperature-dependent excitonic photoluminescence of hybrid organometal halide perovskite films, Phys. Chem. Chem. Phys. **16**, 22476–22481 (2014), https://doi.org/10.1039/C4CP03573A

[20] S. Zhuang, D. Xu, J. Xu, B. Wu, Y. Zhang, X. Dong, G. Li, B. Zhang, and G. Du, Temperature-dependent photoluminescence on organic inorganic metal halide perovskite $CH_3NH_3PbI_{3-x}Cl_x$ prepared on ZnO/FTO substrates using a two-step method, Chin. Phys. B **26**(1), 017802 (2017), https://doi.org/10.1088/1367-2630/19/1/017802

[21] T. Liu, K. Chen, Q. Hu, R. Zhu, and Q. Gong, Inverted perovskite solar cells: progresses and perspectives, Adv. Energy Mater. **6**(17), 1600457 (2016), https://doi.org/10.1002/aenm.201600457

[22] C.-Y. Chen, J.-H. Chang, K.-M. Chiang, H.-L. Lin, S.-Y. Hsiao, and H.-W. Lin, Perovskite photovoltaics for dim-light applications, Adv. Funct. Mater. **25**(45), 7064–7070 (2015), https://doi.org/10.1002/adfm.201503448

[23] Y.-C. Wang, X. Li, L. Zhu, X. Liu, W. Zhang, and J. Fang, Efficient and hysteresis-free perovskite solar cells based on a solution processable polar fullerene electron transport layer, Adv. Energy Mater. **7**(21), 1701144 (2017), https://doi.org/10.1002/aenm.201701144

[24] A. Giuri, S. Masi, S. Colella, A. Kovtun, S. Dell'Elce, E. Treossi, A. Liscio, C. Esposito Corcione, A. Rizzo, and A. Listorti, Cooperative effect of GO and glucose on PEDOT:PSS for high V_{OC} and hysteresis-free solution-processed perovskite solar cells, Adv. Funct. Mater. **26**(38), 6985–6994 (2016), https://doi.org/10.1002/adfm.201603023

[25] W. Ke, G. Fang, Q. Liu, L. Xiong, P. Qin, H. Tao, J. Wang, H. Lei, B. Li, J. Wan, G. Yang, and Y. Yan, Low-temperature solution-processed tin oxide as an alternative electron transporting layer for efficient perovskite solar cells, J. Am. Chem. Soc. **137**(21), 6730–6733 (2015), https://doi.org/10.1021/jacs.5b01994

[26] J.H. Lee, Y.W. Noh, I.S. Jin, S.H. Park, and J.W. Jung, Efficient perovskite solar cells with negligible hysteresis achieved by sol–gel-driven spinel nickel cobalt oxide thin films as the hole transport layer, J. Mater. Chem. C **7**, 7288–7298 (2019), https://doi.org/10.1039/C9TC00902G

[27] X. Yao, W. Xu, X. Huang, J. Qi, Q. Yin, X. Jiang, F. Huang, X. Gong, and Y. Cao, Solution-processed vanadium oxide thin film as the hole extraction layer for efficient hysteresis-free perovskite hybrid solar cells, Org. Electron. **47**(C), 85–93 (2017), https://doi.org/10.1016/j.orgel.2017.05.006

[28] D. Hong, J. Li, S. Wan, I.G. Scheblykin, and Y. Tian, Red-shifted photoluminescence from crystal edges due to carrier redistribution and reabsorption in lead triiodide perovskites, J. Phys. Chem. C **123**(19), 12521–12526 (2019), https://doi.org/10.1021/acs.jpcc.9b03647

[29] M.A. Reshchikov, Temperature dependence of defect-related photoluminescence in III–V and II–VI semiconductors, J. Appl. Phys. **115**(1), 012010 (2014), https://doi.org/10.1063/1.4838038

[30] M. Leroux, N. Grandjean, B. Beaumont, G. Nataf, F. Semond, J. Massies, and P. Gibart, Temperature quenching of photoluminescence intensities in undoped and doped GaN, J. Appl. Phys. **86**(7), 3721–3728 (1999), https://doi.org/10.1063/1.371242

[31] F. Cheng, S. Hu, L. Chen, Y. Lee, G. Yin, K. Tiong, and J. Shen, Time-resolved photoluminescence studies on localization effects in orthorhombic phase of $CH_3NH_3PbI_3$ perovskite thin film, J. Lumin. **197**, 248–251 (2018), https://doi.org/10.1016/j.jlumin.2018.01.054

[32] F. Ruf, M.F. Aygüler, N. Giesbrecht, B. Rendenbach, A. Magin, P. Docampo, H. Kalt, and M. Hetterich, Temperature-dependent studies of exciton binding energy and phase-transition suppression in (Cs, FA, MA)Pb(I, Br)$_3$ perovskites, APL Mater. **7**(3), 031113 (2019), https://doi.org/10.1063/1.5083792

[33] R. Mackevičiūtė, Š. Bagdzevičius, M. Ivanov, B. Fraygola, R. Grigalaitis, N. Setter, and J. Banys,

Strain engineering of electrical conductivity in epitaxial thin $Ba_{0.7}Sr_{0.3}TiO_3$ film heterostructures, Lith. J. Phys. **56**(3), 173–181 (2016), https://doi.org/10.3952/physics.v56i3.3366

[34] Š. Masys and V. Jonauskas, The crystalline structure of $SrRuO_3$: Application of hybrid scheme to the density functionals revised for solids, Lith. J. Phys. **57**(2), 78–87 (2017), https://doi.org/10.3952/physics.v57i2.3514

[35] T. Schmidt, K. Lischka, and W. Zulehner, Excitation-power dependence of the near-band-edge photoluminescence of semiconductors, Phys. Rev. B **45**, 8989–8994 (1992), https://doi.org/10.1103/PhysRevB.45.8989

[36] H. Shibata, M. Sakai, A. Yamada, K. Matsubara, K. Sakurai, H. Tampo, S. Ishizuka, K.-Kim, and S. Niki, Excitation-power dependence of free exciton photoluminescence of semiconductors, Jpn. J. Appl. Phys. **44**(8), 6113–6114 (2005), https://doi.org/10.1143/jjap.44.6113

[37] Y.-S. Yoo, T.-M. Roh, J.-H. Na, S.J. Son, and Y.-H. Cho, Simple analysis method for determining internal quantum efficiency and relative recombination ratios in light emitting diodes, Appl. Phys. Lett. **102**(21), 211107 (2013), https://doi.org/10.1063/1.4807485

[38] D. Ding, S.R. Johnson, J.B. Wang, S.Q. Yu, and Y.H. Zhang, Determination of spontaneous emission quantum efficiency in InGaAs/GaAs quantum well structures, Proc. SPIE **6841**, 68410D (2007), https://doi.org/10.1117/12.759592

[39] S.R. Johnson, D. Ding, J.-B. Wang, S.-Q. Yu, and Y.-H. Zhang, Excitation dependent photoluminescence measurements of the nonradiative lifetime and quantum efficiency in GaAs, J. Vac. Sci. Technol. B **25**(3), 1077–1082 (2007), https://doi.org/10.1116/1.2720864

[40] X. Yang, X. Yan, W. Wang, X. Zhu, H. Li, W. Ma, and C. Sheng, Light induced metastable modification of optical properties in $CH_3NH_3PbI_{3-x}Br_x$ perovskite films: Two-step mechanism, Org. Electron. **34**, 79–83 (2016), https://doi.org/10.1016/j.orgel.2016.04.020

[41] I. Dursun, Y. Zheng, T. Guo, M. De Bastiani, B. Turedi, L. Sinatra, M.A. Haque, B. Sun, A.A. Zhumekenov, M.I. Saidaminov, F.P. García de Arquer, E.H. Sargent, T. Wu, Y.N. Gartstein, O.M. Bakr, O.F. Mohammed, and A.V. Malko, Efficient photon recycling and radiation trapping in cesium lead halide perovskite waveguides, ACS Energy Lett. **3**(7), 1492–1498 (2018), https://doi.org/10.1021/acsenergylett.8b00758

[42] A.J. Knight, A.D. Wright, J.B. Patel, D.P. McMeekin, H.J. Snaith, M.B. Johnston, and M. Herz, Electronic traps and phase segregation in lead mixed-halide perovskite, ACS Energy Lett. **4**(1), 75–84 (2019), https://doi.org/10.1021/acsenergylett.8b02002

[43] B. Zhang, F. Guo, J. Xue, L. Yang, Y. Zhao, M. Ge, Q. Cai, B. Liu, Z. Xie, D. Chen, H. Lu, R. Zhang, and Y. Zheng, Photoluminescence study of the photoinduced phase separation in mixed-halide hybrid perovskite $CH_3NH_3Pb(Br_xI_{1-x})_3$ crystals synthesized via a solvothermal method, Sci. Rep. **7**(1), 17695 (2017), https://doi.org/10.1038/s41598-017-18110-6

[44] A. Sadhanala, F. Deschler, T.H. Thomas, S.E. Dutton, K.C. Goedel, F.C. Hanusch, M.L. Lai, U. Steiner, T. Bein, P. Docampo, D. Cahen, and R.H. Friend, Preparation of single-phase films of $CH_3NH_3Pb(I_{1-x}Br_x)_3$ with sharp optical band edges, J. Phys. Chem. Lett. **5**(15), 2501–2505 (2014), pMID: 26277936, https://doi.org/10.1021/jz501332v

[45] A.A. Mamun, T.T. Ava, H.J. Jeong, M.S. Jeong, and G. Namkoong, A deconvoluted PL approach to probe the charge carrier dynamics of the grain interior and grain boundary of a perovskite film for perovskite solar cell applications, Phys. Chem. Chem. Phys. **19**, 9143–9148 (2017), https://doi.org/10.1039/C7CP01140G

[46] D.W. de Quilettes, S.M. Vorpahl, S.D. Stranks, H. Nagaoka, G.E. Eperon, M.E. Ziffer, H.J. Snaith, and D.S. Ginger, Impact of microstructure on local carrier lifetime in perovskite solar cells, Science **348**(6235), 683–686 (2015), https://doi.org/10.1126/science.aaa5333

[47] M. Saliba, T. Matsui, J.-Y. Seo, K. Domanski, J.-P. Correa-Baena, M.K. Nazeeruddin, S.M. Zakeeruddin, W. Tress, A. Abate, A. Hagfeldt, and M. Grätzel, Cesium-containing triple cation perovskite solar cells: improved stability,

reproducibility and high efficiency, Energy Environ. Sci. **9**, 1989–1997 (2016), https://doi.org/10.1039/C5EE03874J

[48] B.-W. Park, S.M. Jain, X. Zhang, A. Hagfeldt, G. Boschloo, and T. Edvinsson, Resonance Raman and excitation energy dependent charge transfer mechanism in halide-substituted hybrid perovskite solar cells, ACS Nano **9**(2), 2088–2101 (2015), pMID: 25668059, https://doi.org/10.1021/nn507345e

[49] P. Sanguino, M. Niehus, L. Melo, R. Schwarz, A. Fedorov, J. Martinho, M. Soares, and T. Monteiro, Photoluminescence decay in the ps time regime and structural properties of pulsed-laser deposited GaN, Phys. B Condens. Matter **340–342**, 457–461 (2003), https://doi.org/10.1016/j.physb.2003.09.035

[50] S. Bharill, P. Sarkar, J.D. Ballin, I. Gryczynski, G.M. Wilson, and Z. Gryczynski, Fluorescence intensity decays of 2-aminopurine solutions: Lifetime distribution approach, Anal. Biochem. **377**(2), 141–149 (2008), https://doi.org/10.1016/j.ab.2008.03.034

[51] J.M. Remington, A.M. Philip, M. Hariharan, and B. Kohler, On the origin of multiexponential fluorescence decays from 2-aminopurine-labeled dinucleotides, J. Chem. Phys. **145**(15), 155101 (2016), https://doi.org/10.1063/1.4964718

[52] H. He, Q. Yu, H. Li, J. Li, J. Si, Y. Jin, N. Wang, J. Wang, J. He, X. Wang, Y. Zhang, and Z. Ye, Exciton localization in solution-processed organolead trihalide perovskites, Nat. Commun. **7**(1), 10896 (2016), https://doi.org/10.1038/ncomms10896

[53] M.N. Berberan-Santos, A luminescence decay function encompassing the stretched exponential and the compressed hyperbola, Chem. Phys. Lett. **460**(1), 146–150 (2008), https://doi.org/10.1016/j.cplett.2008.06.023

[54] A. Zatryb, G. Podhorodecki, J. Misiewicz, J. Cardin, and F. Gourbilleau, On the nature of the stretched exponential photoluminescence decay for silicon nanocrystals, Nanoscale Res. Lett. **6**(1), 106 (2011), https://doi.org/10.1186/1556-276X-6-106

[55] B.J. Pernick, Luminescent processes and decay laws in crystalline materials, Appl. Opt. **1**(6), 753–758 (1962), https://doi.org/10.1364/AO.1.000753

[56] M. Berberan-Santos, E. Bodunov, and B. Valeur, Mathematical functions for the analysis of luminescence decays with underlying distributions: 2. Becquerel (compressed hyperbola) and related decay functions, Chem. Phys. **317**(1), 57–62 (2005), https://doi.org/10.1016/j.chemphys.2005.05.026

[57] L. Whitehead, R. Whitehead, B. Valeur, and M. Berberan-Santos, A simple function for the description of near-exponential decays: The stretched or compressed hyperbola, Am. J. Phys. **77**(2), 173–179 (2009), https://doi.org/10.1119/1.3008007

[58] P. Strak, K. Koronski, K. Sobczak, J. Borysiuk, K.P. Korona, K. Sakowski, A. Suchocki, E. Monroy, S. Krukowski, and A. Kaminska, Exact method of determination of the recombination mode from time resolved photoluminescence data, arXiv:1709.05249v4 (2019), https://arxiv.org/abs/1709.05249v4

HIBRIDINIŲ PEROVSKITŲ FOTOLIUMINESCENCIJOS SAVYBĖS SAULĖS ELEMENTUOSE SU TiO_2 IR $Mg_{0.2}Zn_{0.8}O$ ELEKTRONŲ PERNAŠOS SLUOKSNIAIS

A. Čerškus [a, b], S. Ašmontas [a], K. Petrauskas [a], A. Sužiedėlis [a], J. Gradauskas [a, b], A.S. Opanasyuk [c], B. Vengalis [a]

[a] *Fizinių ir technologijos mokslų centras, Vilnius, Lietuva*
[b] *Vilniaus Gedimino technikos universitetas, Vilnius, Lietuva*
[c] *Valstybinis Sumų universitetas, Sumai, Ukraina*

Santrauka

Pateikiami perovskitų sluoksnių, nusodintų centrifuginio dengimo metodu ant titano dioksido ir cinko magnio oksido kaip elektronų pernašos sluoksnių, fotoliuminescencijos savybių tyrimai. Ištirta liuminescencijos priklausomybė nuo temperatūros ir žadinimo intensyvumo bei liuminescencijos gesimo kinetika. Be to, darbe aptariami galimi krūvininkų rekombinacijos mechanizmai. Sudėtingas liuminescencijos gesimas buvo aproksimuotas keliais modeliais, tačiau tik keturių eksponenčių ir dviejų hiperbolinių funkcijų sumos modelis geriausiai aprašo eksperimentinius rezultatus. Pirmas bandymas pakeisti titano dioksidą magnio cinko oksidu pagerino perovskito optines savybes: sumažėjo nespindulinė rekombinacija ir pailgėjo gesimo trukmė.